Comparative Study on Dynamic Characteristics of Two-Stage Gear System With Gear and Shaft Cracks Considering the Shaft Flexibility

YONG SHEN, XIANGFENG ZHANG, HONG JIANG, JIANXING ZHOU, SHUAI QIAO, CHENGLONG WANG, AND TONGWEI MA
College of Mechanical Engineering, Xinjiang University, Urumqi 830047, China

Corresponding authors: Xiangfeng Zhang (15276606076@163.com) and Hong Jiang (onlyxjjh@xju.edu.cn)

ABSTRACT To analyze the vibration characteristic differences of a gear transmission system with gear and shaft cracks, an improved computational method for deriving the shaft stiffness matrix with breathing cracks is developed. Also, the three-dimensional contact model of spur gear with a crack is established via the finite element method (FEM), and its meshing stiffness is calculated. Simultaneously, considering bearing stiffness and shaft flexibility, the finite element dynamic models of two-stage gear transmission system with gear and shaft cracks are established. Based on this, different source fault vibration responses are compared and the influencing factors are explored. In addition, a novel signal processing method based on the particle swarm optimization, maximum correlated kurtosis deconvolution, variational, mode decomposition and fast spectral kurtosis (PSO-MCKD-VMD-FSK) is utilized to extract fault characteristics for the signal-to-noise ratio and uneven energy distribution problems. Results show that a system with gear cracks mainly presents periodic impact in the time domain, while in the frequency domain it impacts rotation frequency modulation near the meshing frequency and its multiple frequencies. However, the shaft crack breathing effect meant that the time domain mainly presents ''simple harmonic'' modulation, and the rotation frequency and its faulty shaft multiplication occurs in the low-frequency region of the frequency domain. The PSO-MCKD-VMD-FSK method extracts fault features in a strong noise environment and has good robustness. Results identify different source faults and provide a theoretical basis.

INDEX TERMS Gear transmission system, vibration response, gear crack, shaft crack, fault diagnosis.

NOMENCLATURE

r_p	Base circle radius of the driving gear
r_g	Base circle radius of the driven gear
α	Pressure angle
$\mathbf{K_m}$	Meshing stiffness matrix
$\mathbf{C_m}$	Meshing damping matrix
m_p, m_g	Mass of gear
I_p, I_g	Moment of inertia of gear
q_o	Crack depth
f_s	Normal impact force of gear pair
f	Contact force of gear pair
r_n	Inner ring radius of driving gear

k_m	Meshing stiffness
$\mathbf{M_e}$	Mass matrix of shaft element
$\mathbf{C_e}$	Damping matrix of shaft element
$\mathbf{K_e}$	Stiffness matrix of shaft element
Ω	Input speed
$\mathbf{K_c(t)}$	Stiffness matrix of shaft element with crack
$\mathbf{K_c^d}$	Stiffness reduction t matrix of crack shaft
α_o	Circumferential angle of crack
e	Eccentricity of the crack section
r	Shaft radius
I_v^O, I_w^O	The moment of inertia of crack part for Ov and Ow
I_p^O	The pole inertia moment of crack part for O

$I_{v'}^{O'}, I_{w'}^{O'}$	The moment of inertia of crack part for $O'v'$ and $O'w'$
$I_{p'}^{O'}$	The pole inertia moment of crack part for O'
λ_g	Dimensionless crack depth for gear crack
λ_s	Dimensionless crack depth for shaft crack
M	Mass assembly matrix
C	Damping assembly matrix
$\mathbf{K_f}$	Stiffness assembly matrix
f_{ni}	The system natural frequency
f_{ti}	Rotation frequency
f_{mi}	Meshing frequency

I. INTRODUCTION

The gear transmission system has the advantages of high precision, efficiency, stability, etc. as well as being is widely used in aerospace, transportation, energy equipment and other fields. However, the gear transmission system structure is becoming more complicated, and the working environment remains relatively harsh, so the gear transmission is prone to various failures throughout its life cycle. Among them, cracks are the most common failure mode, whether it be for gears or shafts. Different fault sources will cause different vibration characteristics in the system. Therefore, analyzing the vibration characteristics of cracks in different fault sources for fault location and diagnosis is greatly significant.

At this point, much research has been carried out on gear and shaft cracks of rotating machinery. Studies [1], [2] have shown that, gear meshing stiffness reduction is an important index for measuring the degree of gear damage. Howard *et al.* [3] used the finite element software to calculate the meshing stiffness of gear pair with cracks, and established the torsional vibration model of single stage reducer. Yang *et al.* [4] calculated the meshing stiffness of gear pair by potential energy method. On this basis, Tian *et al.* [5] further modified the algorithm by considering the influence of shear energy on the meshing stiffness of gears, and calculated and compared the time-varying mesh stiffness (TVMS) of missing tooth, cracked tooth and broken tooth. Then, Litak [6] obtained the meshing stiffness of gear with fault by analytical method, and obtained the dynamic characteristics of single degree of freedom gear transmission system with fault. After that, Wu *et al.* [7] established a 6-DOF gear system dynamic model considering the lateral vibration of the gear, and studied the vibration characteristics of the transmission system with crack. Meng *et al.* [8] calculated the meshing stiffness of gear under the failure of tooth surface spalling and crack by potential energy method, and analyzed the fault characteristics. To sum up, at present, there are various and more accurate methods to solve the time-varying meshing stiffness, but most of the gear transmission systems use the lumped mass method to establish the model, ignoring the flexibility of the transmission shaft, so that the final solution error is large. In order to solve the above problems, Saxena *et al.* [9] established a dynamic model of single-stage gear transmission system based on the finite element method. The

results show that the system response is more practical after considering the shaft flexibility.

The literature mentioned above shows the extensiveness of research on the dynamic response of the gear transmission system with gear failures. In contrast, the dynamic response of the gear transmission system with shaft cracks have not been fully studied, but the dynamics of bearing-rotor system with crack has a certain foundation. As early as 1976, Gasch [10] utilized the hinge spring model to simulate the simple solid shaft cracked rotor system and analyzed its vibration characteristics. Then, Dimarogonas *et al.* [11] found that the change of the vibration characteristics of a cracked rotor is caused by the changing of the stiffness matrix of the rotor. Mayes *et al.* [12] proposed to use the cosine model to simulate crack opening and closing law. After that, a breathing model was established in [13], [14] to simulate the opening and closing law of cracks. Patel [15] studied the influence of crack breathing effect on its vibration characteristics. Al-shudeifat *et al.* [16], [17] considered the time-varying product of the inertia and the moment of inertia of the crack section, thereby derived a new stiffness model of the cracked rotor, and verified the model through experiments. Based on this, Lu *et al.* [18] studied the vibration characteristics of a double rotor system with a breathing crack. In conclusion, past research, the research on the fault of the common rotor system is more concentrated. However, research on the gear coupling system is relatively limited.

Scholars have also researched crack fault diagnosis. To solve the lack of adaptability of traditional signal analysis methods and the inability to extract effective fault-feature information from strong noise and nonlinear vibration signals, scholars have proposed a series of signal processing methods that are widely used in gear system fault diagnosis. For example, Yu *et al.* [19] combined empirical mode decomposition (EMD) with the autoregressive (AR) model to extract effectively the feature vector of a gear fault; Cheng *et al.* [20] combined local mean decomposition (LMD) and spectral kurtosis (spectral kurtosis) (SK) to identify gear faults. However, EMD and LMD belong to recursive mode decomposition, resulting in some unavoidable problems, such as mode mixing, the end effect, the boundary effect and so on [21], [22]. In recent years, Dragomiretskiy *et al.* [23] proposed VMD, which can not only avoid EMD and LMD shortcomings, but also has good robustness to noise. Simultaneously, McDonald *et al.* [24] proposed the MCKD algorithm. Through the deconvolution operation, MCKD highlights the continuous impulse submerged by noise and improves the correlation kurtosis of the original signal. It is suitable for extracting the continuous transient impulse of a weak fault signal. FSK, proposed by Antoni [25], can accurately reflect the instantaneous impact component of the vibration signal in strong noise, thereby quickly selecting the best filter.

In summary, previous research shows that relatively few studies focus on the shaft fault of a gear system, and the centralized mass method is often utilized for modeling of gear

transmission system with fault; therefore, transmission shaft flexibility is not effectively taken into account.

In this work, to analyze the vibration characteristic differences of a gear transmission system with gear and shaft cracks, first, the time-varying meshing stiffness of a gear crack fault was solved via FEM and the stiffness of the shaft section with a breathing crack was derived. Second, considering the shaft flexibility, the two-stage gear drive system with gear and shaft cracks were established respectively and its vibration characteristics were studied. Finally, test data was collected and the fault characteristic frequency is processed by PSO-MCKD-VMD-FSK method.

II. FINITE ELEMENT MODEL OF GEAR TRANSMISSION SYSTEM

A. MODEL OF TWO-STAGE GEAR TRANSMISSION SYSTEM

In this study, the transmission system of a two-stage spur gear reducer is taken as the research object. The transmission system consists of three shafts, two pairs of gear pairs and three pairs of bearings. In order to improve the accuracy of solution of bearing vibration response and fault vibration signal, taking into account the flexibility of shaft section, the finite element model of transmission system is established as shown in Figure 1. And the model is divided into 32 nodes and 29 elements by using shaft element, gear meshing element and bearing shaft element. Bearing nodes are respectively located at nodes 5, 13, 14, 22, 23 and 31, gear nodes are located at nodes 7, 16, 20 and 29, among which node 7 and node 16 constitute the first stage mesh element, node 20 and node 29 constitute the second stage gear mesh element.

B. DYNAMIC MODEL OF GEAR MESHING ELEMENT WITH CRACK

One of the main causes of vibration and noise of gear box is the periodic change of meshing stiffness of gear, during the gear transmission. At the same time, gear failure will reduce the meshing stiffness of the gear, resulting in abnormal vibration of the gearbox. Therefore, the establishment of the dynamic model of the gear with tooth root crack can provide a theoretical basis for the fault diagnosis of the gearbox.

1) DYNAMIC MODEL OF NORMAL GEAR MESHING ELEMENT

The basic parameters of the gear pair are shown in Table 1, Considering the influence of time-varying meshing stiffness $K_m(t)$ and transmission error $e(t)$, a 6-DOF meshing element dynamic model of spur gear is established as shown in Figure 2. In Figure 2, w_p, w_g, v_p and v_g are the degrees of freedom of the lateral vibration of the gear pair, and θ_p and θ_g are the degrees of freedom of the torsional vibration of the gear pair.

The vibration displacement of the gear pair in each direction is projected in the direction of the meshing line to obtain the relative total deformation δ:

$$\delta = v_p \sin\alpha + w_p \cos\alpha - r_p\theta_p - v_g\sin\alpha - w_g \cos\alpha - r_g\theta_g - e(t) \quad (1)$$
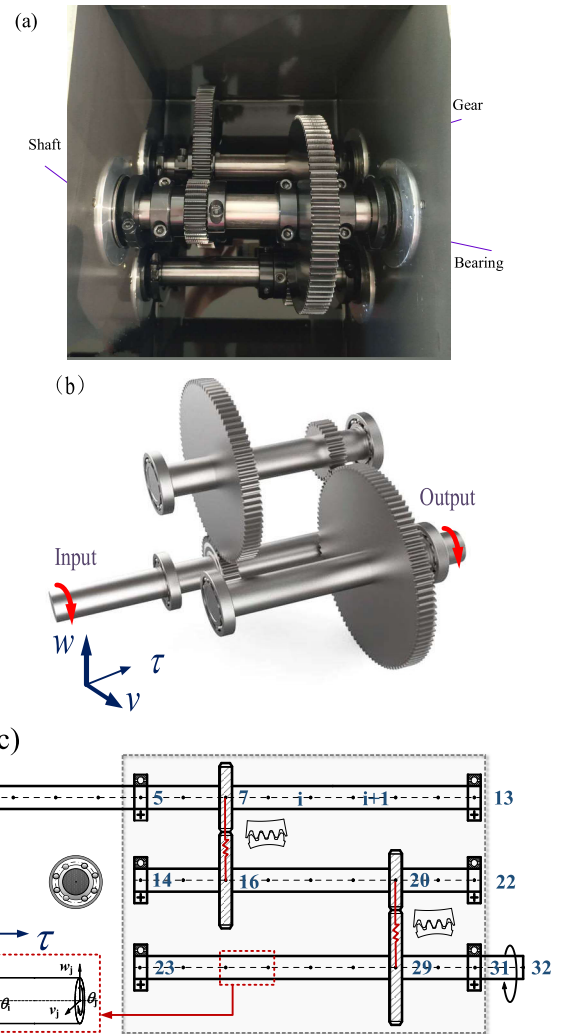

FIGURE 1. (a) Internal structure diagram of experimental gearbox. (b) Assembly model of two-stage gear transmission system. (c) Finite element model of two-stage gear transmission system.

TABLE 1. Parameters of gear.

Parameter	1st stage driving gear	1st stage driven gear	2nd stage driving gear	2nd stage driven gear
Number of teeth	36	90	29	100
Module(mm)	1.5	1.5	1.5	1.5
Pressure angle(°)	20	20	20	20
Moment of inertia (kg.m²)	2×10⁻⁴	3.04×10⁻³	1×10⁻⁴	8.71×10⁻³
Tooth width (mm)	12	12	12	12
Mass (kg)	0.16	1.3	0.09	1.6

where, r_p and r_g are the base circle radius of the driving gear and the driven gear, respectively, and α is the pressure angle.

Therefore, the gear meshing force can be expressed as

$$F_m = K_m(t)\delta + C_m\dot{\delta} \quad (2)$$

here, $\boldsymbol{K_m}$ is meshing stiffness, $\boldsymbol{C_m}$ is meshing damping.
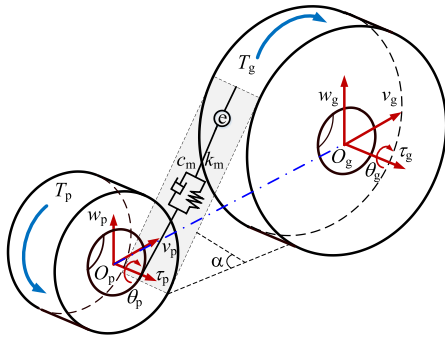
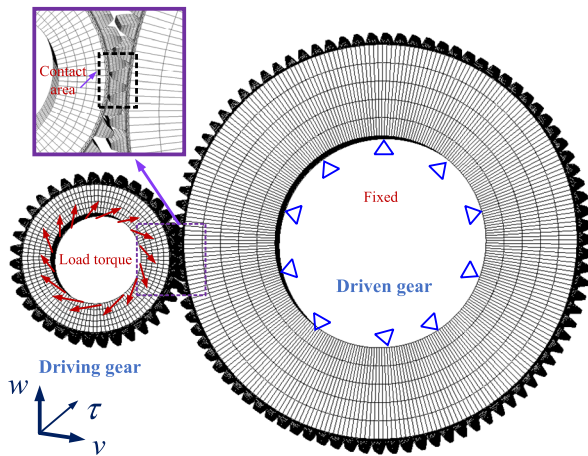**FIGURE 2.** Dynamics model of meshing gear pair.

FIGURE 3. Calculation of meshing stiffness.

According to the D'alembert's principle, the differential equation of motion of the gear meshing element is expressed as

$$
\begin{cases}
m_p \ddot{v}_p + c_m \dot{\delta} \sin\alpha + k_m \delta \sin\alpha + f_s \sin\alpha = 0 \\
m_p \ddot{w}_p + c_m \dot{\delta} \cos\alpha + k_m \delta \cos\alpha + f_s \cos\alpha = 0 \\
I_p \ddot{\theta}_p - c_m \dot{\delta} r_p - k_m \delta r_p - f_s r_p = 0 \\
m_g \ddot{v}_g - c_m \dot{\delta} \sin\alpha - k_m \delta \sin\alpha - f_s \sin\alpha = 0 \\
m_g \ddot{w}_g - c_m \dot{\delta} \cos\alpha - k_m \delta \cos\alpha - f_s \cos\alpha = 0 \\
I_g \ddot{\theta}_g - c_m \dot{\delta} r_g - k_m \delta r_g - f_s r_g = 0
\end{cases}
\tag{3}
$$

where, m, I and f_s denote the mass, moment of inertia, normal impact force of gear pair respectively, while the subscripts *p* and *g* represent the pinion and driven gear, respectively.

2) CALCULATION OF MESHING STIFFNESS

Establish the three-dimensional contact model of spur gear, and use the finite element method to solve the meshing stiffness of the transmission system, as shown in Figure 3.

Mesh stiffness is solved under ideal conditions without considering assembly errors, machining errors, and backlash. This model uses a combination of hexahedral elements and tetrahedral elements for meshing which the hexahedron mesh is used to divide teeth and hub and the tetrahedral mesh is used for the transition at the root position. Meanwhile, reduce

the number of meshes appropriately in non-contact areas to improve computational efficiency.

In this study, calculation of contact between teeth by penalty function method. And it is assumed that the two contact points are connected by linear springs. Thus, according to Hooke's law, the permeability relationship between contact points can be expressed as

$$
f = k\mu
\tag{4}
$$

where, f is contact force, k is contact stiffness, and μ is penetration depth, k can be calculated as follows:

$$
k = \frac{f_o M A^2}{V}
\tag{5}
$$

In which, f_o represents penalty coefficient, whose value is generally taken as 0.1. M is bulk modulus of contact element, A is contact element area, V is contact element volume.

In local cylindrical coordinate system, the transverse displacement of the driving wheel is restrained, and then the joint force is applied on the inner ring joint of the gear to realize the load torque on the driving gear. The torque calculation formula is as follows

$$
T = n f_m r_n
\tag{6}
$$

where, n is number of inner ring nodes of driving gear, f_m is circumferential nodal force, r_n is inner ring radius of driving gear.

Therefore, the equivalent force along the meshing line of the gear is

$$
F_b = \frac{T}{r_p}
\tag{7}
$$

here, r_b is base circle radius of driving gear.

In order to avoid the influence of local deformation, the average value of the displacement of all nodes on the inner ring of the driving wheel is used to equivalent the torsional deformation amount *n* of the inner ring of the gear. Thus, the relative angle of the drive gear is expressed as

$$
\theta = \frac{\delta_n}{r_n}
\tag{8}
$$

The equivalent deformation caused by the comprehensive deformation on the meshing line is

$$
\delta_b = \theta r_p
\tag{9}
$$

Finally, the calculation formula of gear meshing stiffness is obtained as follows:

$$
K_m = \frac{n f_m r_n^2}{\delta_n r_p^2}
\tag{10}
$$

Divide the meshing period of a gear tooth of the driving gear into 10 equal parts, adjust the position of the driven gear according to the meshing relationship of the gear pair. On this basis, 10 meshing states of gear pair are obtained, and the corresponding meshing stiffness of 10 meshing states is obtained by repeating the above stiffness calculation steps. Thereafter,
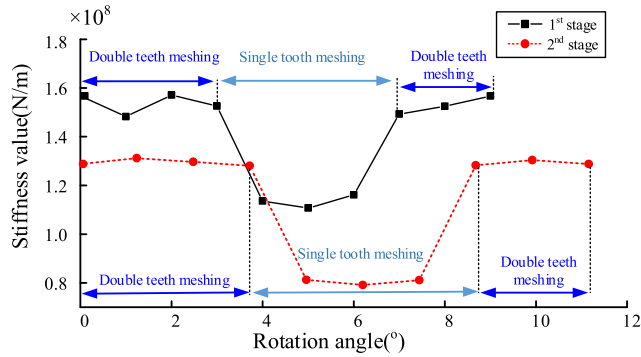
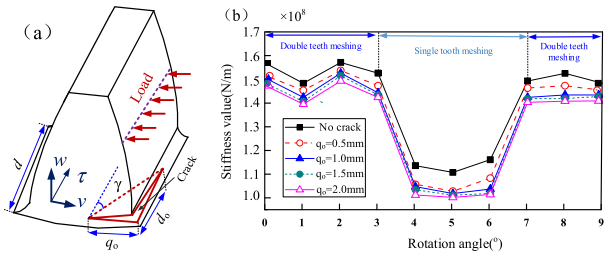**FIGURE 4.** The curve of TVMS without fault.

FIGURE 5. Gear model with root crack fault: (a) gear with root crack fault (b) meshing stiffness curve.

the curve of meshing stiffness of a meshing period is obtained by fitting by interpolation method as shown in Fig.4.

Fig.4 shows the meshing stiffness of double teeth is greater than that of single teeth. The entire meshing cycle is shown as double tooth meshing-single tooth meshing-double tooth meshing alternately, and the meshing time of double teeth is longer than that of single teeth. When the single and double teeth are alternated, there is a step change in the meshing stiffness, which causes the transmission system to present a more obvious stiffness excitation.

3) MODEL OF GEAR CRACK

The gear teeth are constantly subjected to the impact of the meshing force during the meshing process. Due to the stress concentration, cracks are often prone to occur at the root of the meshing surface. Therefore, the structural cracks at the root of the tooth are shown in Figure 5.

In Fig. 5(a), d is the tooth width, d_o is the crack extension length in the tooth width direction, γ is the crack angle, and q_o is the crack depth. Repeat the II.B.2-section meshing stiffness calculation procedure during calculation, and finally get the gear meshing stiffness curve with root crack as shown in Figure 5(b). As shown in Figure 5(b), when a crack failure occurs on the first-stage gear pair driving wheel ($\gamma = 15°$), the stiffness change curve of the faulty tooth during the meshing period. Compared with the time-varying meshing stiffness of healthy gears, it can be seen that due to the presence of cracks, the flexibility of the gear teeth is increased and the meshing stiffness is reduced. As the depth of the crack expands, the meshing stiffness of the system also tends

TABLE 2. Parameters of shaft.

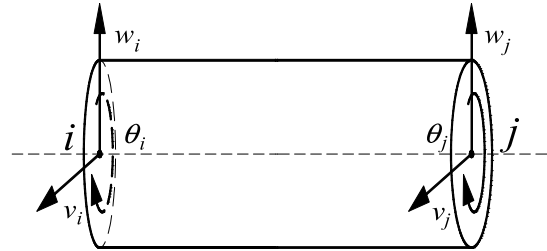| Parameter	Input shaft	Countershaft	Output shaft
Length (m)	0.24	0.16	0.18
Radius (mm)	10	10	10
Density (kg/m^3)	7850	7850	7850
Shear modulus (Pa)	8×10^{10}	8×10^{10}	8×10^{10}
Elastic modulus (Pa)	2.1×10^{11}	2.1×10^{11}	2.1×10^{11}

FIGURE 6. Schematic diagram of shaft element.

to decrease, and the effect of the crack on the single-teeth meshing area is more significant than that of the double-teeth meshing area. Due to the existence of cracks, the meshing stiffness of the gear appears to be periodically weakened, so that the system vibration signal exhibits periodic impact.

C. MODEL OF SHAFT ELEMENT WITH CRACK
1) MODEL OF HEALTHY SHAFT ELEMENT
In the spur gear transmission system, the rotating shaft is mainly subjected to the external force torque and the radial load generated by the gear transmission. The parameters of the transmission shaft are shown in Table 2. Considering the influence of shear deformation, a simple space beam element model is constructed by combining Timoshenko beam theory as shown in Figure 6.

Each node of the model considers three degrees of freedom, including degrees of freedom of translation in w and v directions and degrees of freedom of torsion in α direction. Thus the differential equation of motion of the shaft segment element is expressed as:

$$M_e \ddot{X}_e + C_e \dot{X}_e + K_e X_e = 0 \tag{11}$$

where, $X_e = \{v_i, w_i, \theta_i, v_j, w_j, \theta_j\}^T$ represents the displacement column vector of the shaft element; M_e is the mass matrix of the shaft element; K_e is the stiffness matrix of the shaft element; C_e is shaft element damping matrix, calculated by Rayleigh damping

$$C_e = \alpha \cdot M_e + \beta \cdot K_e \tag{12}$$

here, α and β are Rayleigh damping proportional coefficients.

2) CRACKED SHAFT ELEMENT MODELING
During the operation of the gear transmission system, the crack of the shaft is affected by the gravity and the rotation movement, which results in the time-varying stiffness of the
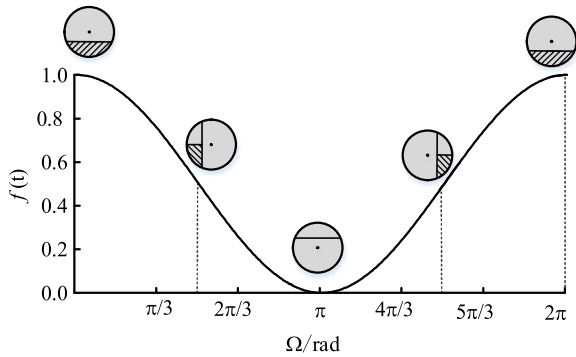
FIGURE 7. Breathing crack model.

cracked shaft element. When the crack is closed, the crack shaft element stiffness can be approximated to the normal shaft element stiffness. When the crack is in the fully open state, the stiffness reduction of crack shaft element reaches the maximum. While in the operation of the equipment, the cracks are more in the transition state. During this period, the amount of stiffness reduction continuously changes with time. In view of the time-varying stiffness of crack shaft element, cosine model is used to simulate the opening and closing law of crack.

$$f(t) = 0.5(1 + \cos(\Omega t)) \quad (13)$$

where, Ω is the input speed of the system, and the opening and closing rules are shown in Figure 7.

The stiffness of crack shaft element can be expressed as

$$K_c(t) = K_e - f(t)K_c^d \quad (14)$$

where $K_c(t)$ is the time-varying stiffness matrix of the crack shaft element, and K_c^d is the stiffness reduction amount of the crack shaft element.

The schematic diagram of crack section is shown in Figure 8, and the shaded part indicates the cracked part. O-vw is the fixed coordinate system with the original center of the shaft as the coordinate origin, where the coordinate origin O is the centroid of the section of the shaft without crack, O'-$v'w'$ is the fixed coordinate system with the new centroid of the shaft after crack as the coordinate origin, and O' is the centroid of the eccentric section of the crack. α_o is the circumferential angle of the crack, e is the eccentricity of the crack cross section relative to the original centroid, h is the crack depth, r is the radius of the rotating shaft, and the dimensionless crack depth $\lambda_s = h/2r$.

A_c represents the area of the crack section, and the area of the area of the crack-free section is A_r, so

$$A_r = \pi r^2 - A_c \quad (15)$$

Among them,

$$A_c = R^2\alpha_o + \sqrt{2Rh - h^2}(R - h) \quad (16)$$
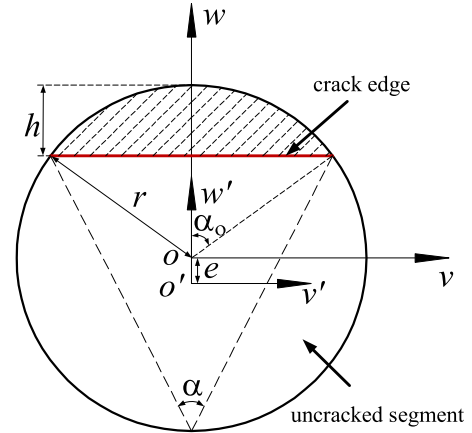
$$\alpha_o = arccos((r - h)/r) \quad (17)$$

FIGURE 8. Schematic diagram of the cracked element cross section.

The eccentricity of the crack section is

$$e = \frac{2r^3}{3A_r}(\frac{2hr - h^2}{r^2})^{3/2} \quad (18)$$

As the crack propagates, the moment of inertia and the moment of polar inertia of the crack part also change. The moment of inertia of the crack part to the coordinate axis and to the origin of the fixed coordinate system are expressed as follows

$$I_v^O = 2 \int_{r-h}^{r} w^2\sqrt{r^2 - w^2}dw \quad (19)$$

$$I_w^O = 2 \int_{0}^{\sqrt{2rh-h^2}} v^2(\sqrt{r^2 - v^2} - r + h)dv \quad (20)$$

$$I_p^O = I_v^O + I_w^O \quad (21)$$

Use the Simpson formula to convert the above integral formula as follows

$$I_v^O = \frac{h}{3}[\sqrt{2hr - h^2}(r-h)^2 + \frac{1}{2}\sqrt{4hr - h^2}(2r - h)^2] \quad (22)$$

$$I_w^O = \frac{2hr - h^2}{3}(\frac{1}{2}\sqrt{4r^2 - 2hr + h^2} - r + h) \quad (23)$$

Considering the effect of the crack on the centroid, combined with the parallel shift axis theorem, the moments of inertia $I_{v'}^{O'}$, $I_{w'}^{O'}$ of the crack part on the coordinate axes $O'v'$ and $O'w'$, and the polar moment of inertia $I_{p'}^{O'}$ of the centroid O' after eccentricity is expressed as follows

$$I_{v'}^{O'} = I_v^O + A_r e^2 \quad (24)$$

$$I_{w'}^{O'} = I_w^O \quad (25)$$

$$I_{p'}^{O'} = I_{v'}^{O'} + I_{w'}^{O'} \quad (26)$$

so, the moment of inertia of the area without crack in the new centroid coordinate system: can be expressed as

$$I_{rv'}^{O'} = \frac{\pi}{4}r^4 - I_{v'}^{O'} \quad (27)$$

$$I_{rw'}^{O'} = \frac{\pi}{4}r^4 - I_{w'}^{O'} \quad (28)$$

TABLE 3. Parameters of bearing.

Diameter of inner race (mm)	Diameter of outer race (mm)	Ball diameter (mm)	Ball number
28.7	46.6	8.7	8
Pitch circle diameter（mm）	Curvature radius (mm)	Radial internal clearance	Goodness fit
37.65	4.5	0.5	0.5172
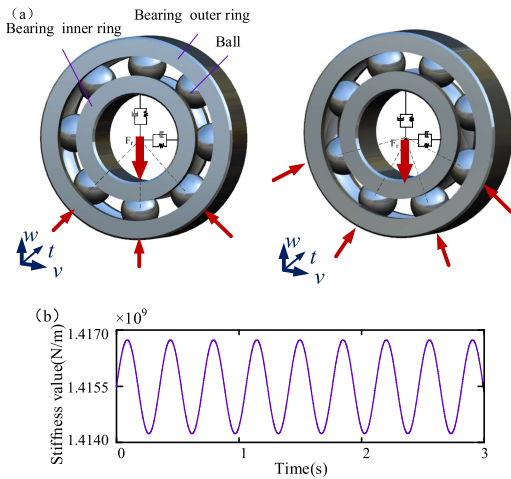
FIGURE 9. (a) Model of the bearing element. (b) The curve of time varying bearing stiffness.

Therefore, the crack element stiffness matrix reduction is expressed as (29), as shown at the bottom of the next page where, $\varphi_v = \frac{12EI_v}{\xi A_r Gl^2}$, $\varphi_w = \frac{12EI_w}{\xi A_r Gl^2}$, G represents 80 Gpa for shear modulus, E is 210 Gpa for elastic modulus and ξ is 4/3 for shear coefficient.

The time-varying stiffness matrix $K_c(t)$ of cracked shaft element can be obtained by substituting stiffness reduction element K_c^d into formula (14).

D. MODEL OF BEARING

In the gear transmission system, the bearing mainly plays a role of supporting the shaft system and reducing the friction coefficient during the movement. The specific parameters are shown in Table 3. During the running of the bearing, the roller passes through the loading area in turn, and the whole process is contact-contact deformation maximum-recovery deformation. In this process, the bearing load can be divided into "odd pressure" and "even pressure", as shown in the figure9.

The radial displacement can be expressed as

$$\delta_r = 4.36 \times 10^{-4} \frac{Q_{max}^{2/3}}{D^{1/3} \cos\alpha} \tag{30}$$

where, Q_{max} is the maximum normal load of the roller "odd pressure", D is the diameter of the roller, and α is the contact angle of the bearing.

The stiffness of bearing under odd pressure is expressed as

$$k_{bo} = \frac{F_r}{\delta_r} \tag{31}$$

here, F_r is the radial load of the bearing.

In the case of even pressure, the load distributed to the azimuth angle of the roller is regarded as the maximum load at this time, and the value is substituted into the formula (31) to obtain the stiffness k_{be} of the bearing under even pressure.

Considering the stiffness distribution of the three groups of deep groove ball bearings in this model as isotropic, $K_v(t)$ and $K_w(t)$ represent the time-varying stiffness of the bearings in the horizontal and vertical directions, respectively.

$$K_{v,w}(t) = K_o + K_a \sin(2\pi f_b t + \beta_o) \tag{32}$$

where, K_o is the bearing static stiffness; K_a is the fluctuation amplitude of bearing stiffness; f_b is the bearing passing frequency; β_o is the bearing phase angle, and $K_o = (k_{bo} + k_{be})/2$.

E. SYSTEM MODEL

Considering the coupling relationship between the elements and the total stiffness matrix bandwidth, the elements are integrated according to the node number. Figure 10 shows the schematic diagram of stiffness assembly. After removing rigid body displacement, the total assembly matrix contains 95 degrees of freedom of nodes, including 38 degrees of freedom of nodes in the input shaft section, 27 degrees of freedom of nodes in the intermediate shaft section, 30 degrees of freedom of nodes in the output shaft section, and 0 elements in the blank.

Figure 10(a) shows the general assembly diagram of the stiffness matrix of the system with a gear crack. As the coupling element of the connecting shaft system, the gear meshing element not only reduces local joint stiffness where the gear is located, but also changes the stiffness value of the coupling position when the gear fails, thus realizing the transmission of the system fault. Figure 10(b) shows a general assembly diagram of the stiffness matrix of the system with a shaft crack, which mainly affects the stiffness values of the element in which the crack is located as compared with gear faults.

Therefore, the dynamic differential equation of the two-stage gear transmission system with crack is expressed as

$$M\ddot{X} + C\dot{X} + K_f X = P_o + F_e \tag{33}$$

where, X represents displacement array of nodes, which is expressed as $\{v_1, w_1, v_2, w_2, \theta_2, \ldots, v_{31}, w_{31}, \theta_{31}, v_{32}, w_{32}, \theta_{32}\}$; M, C and K_f are 95×95 matrices, which respectively represent mass assembly matrix, damping assembly matrix and stiffness assembly matrix of system with cracks, and C is Rayleigh damping, which can be expressed as $C = \kappa M + \iota K_f$; P_o is external excitation of system; F_e is error excitation of system.

III. RESPONSE ANALYSIS
A. MODAL ANALYSIS
Natural frequency is the reflection of system inherent attributes. In order to identify the frequency components of system dynamic response and measure the degree of equipment damage, natural frequency of the system is solved.
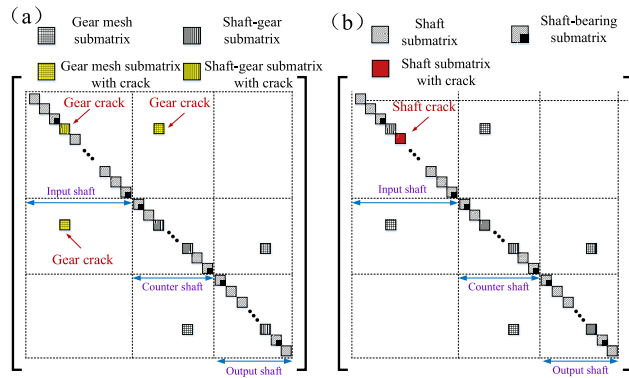
FIGURE 10. Schematic of the assembly rules of the overall system. (a) System considering a crack on the gear. (b) System considering a crack on the shaft.

The system's undamped free vibration equation without external excitation is

$$M\ddot{X} + K_f X = 0 \tag{34}$$

The characteristic equation of the system is thus constructed:

$$|K_f - w_i^2 M| = 0 \tag{35}$$

where, w_i denotes circular frequency.

Convert the system circular frequency w_i into the system natural frequency w_i^n by formula (36)

$$w_i^n = w_i/2\pi \tag{36}$$

Natural frequency of 95orders and corresponding vibration modes of the system are obtained. It is observed that gear failure mainly affects low-order natural frequency while shaft failure mainly affects high-order natural frequency. So, the first 10-order natural frequencies, the 51st to 65th natural frequencies and corresponding vibration modes of the two fault systems are given here as shown in the table 4 and 5.

Tables Table 4 and 5 show how the overall stiffness of the system tends to decrease with the existence of cracks; therefore, the natural system frequency tends to decrease under both faults. Also, as the crack depth increases, the natural frequency reduction amount gradually increases, but the vibration mode corresponding to the natural frequency has not changed. Moreover, gear failure mainly affects the low-order natural frequency of the system, especially the low-order natural frequency corresponding to the torsional vibration mode, such as the changing of the 4th, 7th, 8th, and 10th order natural frequency values, while the 51st to 65th order natural frequency values almost remains unchanged. The difference is that the shaft crack fault has a greater influence on the natural frequencies above the 10th order (including the 10th order), and its effect is not limited to the natural frequencies corresponding to the torsional vibration modes.

B. VIBRATION CHARACTERISTIC ANALYSIS

At an input shaft speed of 50 rad/s and a load of 100N · m., obtained input shaft rotation frequency $f_{t1} = 8.3$Hz, intermediate shaft rotation frequency $f_{t2} = 3.3$Hz, output shaft rotation frequency $f_{t3} = 0.96$Hz, first gear pair meshing frequency $f_{m1} = 299.8$Hz and second gear pair meshing frequency $f_{m2} = 95.7$Hz can be obtained. The dynamic equation of the drive system is solved by Newmark-β and the bearing vibration signal at the right end of the input shaft is extracted as shown in the figure 11.

Figure 11(a) shows the time-domain and frequency-domain diagrams of the transmission system with non-failure. In the frequency domain, the system vibration response is dominated by the meshing frequency and its double frequency, and the first-order natural frequency f_{n1} of the system also exists.

Figure 11(b) shows the vibration response time-domain and frequency-domain diagrams of the 1st stage gear secondary driving gear with a crack; the crack angle is $\gamma = 15°$, and the crack depth is 30%. In the time domain, a clear periodic shock component exists, and the shock period is $1/f_{t1}$. The frequency-domain diagram shows that a sideband is generated near the gear pair meshing frequency and its frequency multiplication, and the side frequency interval is $1/f_{t1}$, where the carrier frequency is the meshing frequency, and the modulation frequency is the input shaft rotation frequency.

$$K_c^d = \begin{bmatrix} \dfrac{12EI_{v'}^{O'}}{(1+\varphi_v)l^3} & 0 & 0 & -\dfrac{12EI_{v'}^{O'}}{(1+\varphi_v)l^3} & 0 & 0 \\ 0 & \dfrac{12EI_{w'}^{O'}}{(1+\varphi_w)l^3} & 0 & 0 & -\dfrac{12EI_{w'}^{O'}}{(1+\varphi_w)l^3} & 0 \\ 0 & 0 & \dfrac{GI_{p'}^{O'}}{l} & 0 & 0 & -\dfrac{GI_{p'}^{O'}}{l} \\ -\dfrac{12EI_{v'}^{O'}}{(1+\varphi_v)l^3} & 0 & 0 & \dfrac{12EI_{v'}^{O'}}{(1+\varphi_v)l^3} & 0 & 0 \\ 0 & -\dfrac{12EI_{w'}^{O'}}{(1+\varphi_w)l^3} & 0 & 0 & \dfrac{12EI_{w'}^{O'}}{(1+\varphi_w)l^3} & 0 \\ 0 & 0 & -\dfrac{GI_{p'}^{O'}}{l} & 0 & 0 & \dfrac{GI_{p'}^{O'}}{l} \end{bmatrix} \tag{29}$$

TABLE 4. Natural frequencies of the system for the first 10 orders.

Mode number	Normal	Gear crack			Shaft crack			Vibration mode
		$\lambda_g = 10\%$	$\lambda_g = 30\%$	$\lambda_g = 50\%$	$\lambda_s = 0.1$	$\lambda_s = 0.3$	$\lambda_s = 0.5$	
1	127.93	127.92	127.89	127.86	127.93	127.93	127.93	Torsion
2	204.58	204.58	204.57	204.57	204.58	204.58	204.58	Torsion
3	1481.74	1481.64	1481.37	1481.17	1481.74	1481.74	1481.73	Torsion
4	1592.50	1590.79	1586.32	1583.23	1592.50	1592.43	1592.33	Torsion
5	1602.55	1602.55	1602.55	1602.55	1602.55	1602.55	1602.55	Translation
6	1760.07	1760.07	1760.06	1760.05	1760.07	1760.07	1760.07	Torsion
7	2869.63	2847.17	2790.48	2753.10	2869.48	2868.12	2865.91	Torsion
8	3159.79	3157.40	3152.75	3150.43	3159.77	3159.58	3159.27	Torsion
9	4587.44	4587.44	4587.44	4587.44	4587.07	4584.05	4577.88	Translation
10	6492.66	6490.80	6461.92	6352.52	6492.25	6079.62	5089.44	Torsion

TABLE 5. Natural frequencies of the system for the 51st to 65th order.

Mode number	Normal	Gear crack			Shaft crack			Vibration mode
		$\lambda_g = 10\%$	$\lambda_g = 30\%$	$\lambda_g = 50\%$	$\lambda_s = 0.1$	$\lambda_s = 0.3$	$\lambda_s = 0.5$	
51	39799.4	39799.16	39798.67	39798.41	39783.81	39631.05	39577.14	Translation
52	41916.81	41916.81	41916.81	41916.81	41916.81	41916.81	41916.812	Translation
53	41916.86	41916.86	41916.86	41916.86	41916.86	41916.86	41916.856	Translation
54	42508.81	42508.81	42508.81	42508.81	42508.81	42508.81	42508.813	Translation
55	42521.11	42521.11	42521.1	42521.1	42521.11	42521.11	42521.108	Translation
56	44141.74	44141.74	44141.74	44141.74	44141.74	44141.74	44141.736	Torsion
57	44143.76	44143.76	44143.76	44143.76	44143.76	44143.76	44143.764	Torsion
58	44148.23	44148.23	44148.23	44148.23	44148.23	44148.23	44148.226	Torsion
59	52213.82	52213.82	52213.82	52213.82	52213.82	51855.14	51023.478	Translation
60	52214.25	52214.22	52214.17	52214.14	52214.25	52213.82	52213.809	Translation
61	53079.09	53079.09	53079.09	53079.09	52777.67	52214.24	52214.24	Torsion
62	53080.78	53080.78	53080.78	53080.77	53079.09	53079.09	53079.091	Torsion
63	56272.57	56272.57	56272.57	56272.57	56272.57	56106.94	55709.954	Translation
64	56272.58	56272.58	56272.58	56272.58	56272.58	56267.36	56130.675	Translation
65	56397.65	56397.65	56397.65	56397.65	56362.71	56272.57	56272.573	Translation

Figure 11(c) shows the time-domain and frequency-domain diagrams of the vibration response of the system with the crack in the gear position ($\lambda_s = 0.3$). Influenced by crack breathing, simple harmonic periodic modulation appears in the time domain, in which the carrier frequency is the meshing frequency and the modulation frequency is the rotating frequency of the input shaft. The long-term component in the time domain is the rotating frequency of rotating shaft (1/T) and the short-term component is the meshing frequency of the gear system. In the frequency domain, f_{t1} and $2f_{t1}$ are clear, and a small amount of side frequency modulation appears near the meshing frequency.

In summary, the time-frequency response differences of the two fault sources include: (1) In the time domain, the transmission system with gear cracks appears as impact signals, while the transmission system with shaft cracks shows "simple harmonic" modulation; (2) The frequency domain shows that the transmission system with gear cracks is mainly manifested as side frequency modulation near the meshing frequency, and the latter mainly exhibits the rotation frequency f_{t1}, $2f_{t1}$, and $3f_{t1}$.

IV. EXPERIMENT
A. SIGNAL ACQUISITION
Spectra Quest comprehensive fault diagnosis test bench is used in this test. As shown in Figure 12, the main drive chain consists of two-stage fixed-shaft gear drive system and single-stage planetary gear drive system. DEWESoft
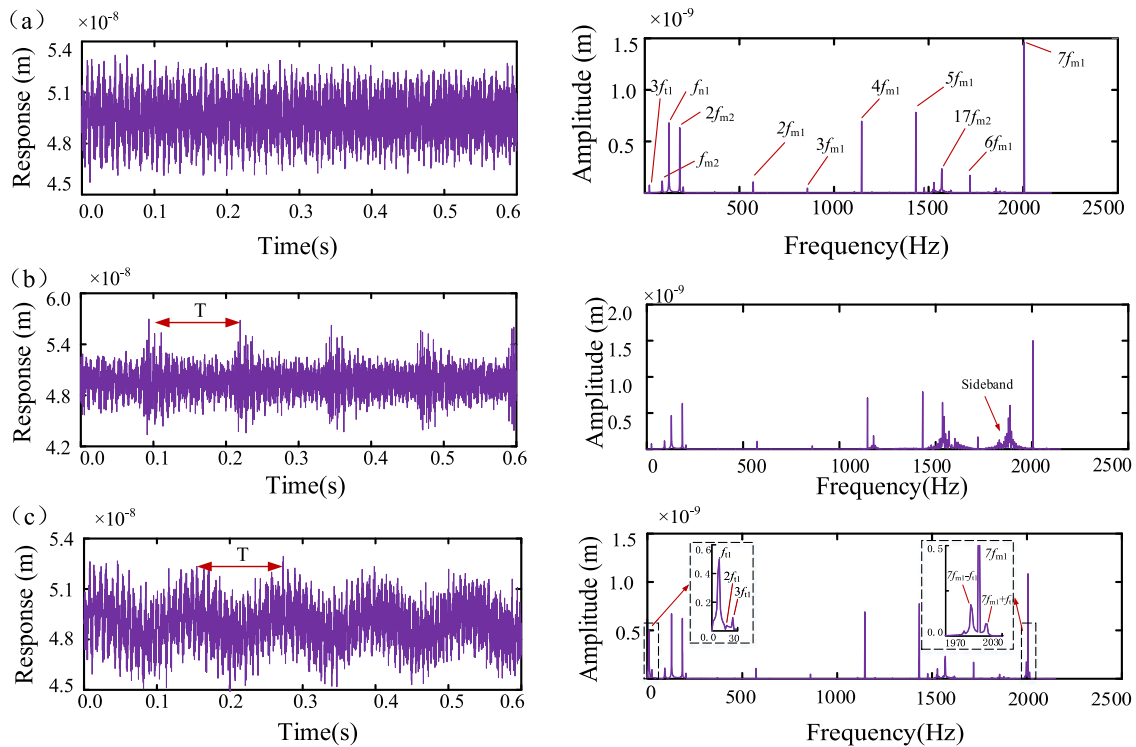
FIGURE 11. Time domain and frequency domain diagrams of the system. (a) Normal system. (b) System with gear crack. (c) System with shaft crack.
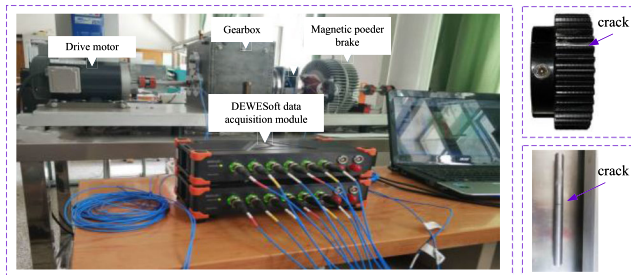

FIGURE 12. Comprehensive test platform for fault diagnosis.

data acquisition system is selected for data acquisition. Prefabricated 2mm crack at tooth root of primary drive gear and input shaft respectively at a speed of 500r/min. The parameters of gear and drive shaft are in accordance with the simulation.

Figure 13 shows the original vibration signals of gear crack and shaft crack collected by the test-bed. The vibration signals appear irregular distribution in time domain. Due to the influence of noise and other factors, the fault characteristics cannot be clearly reflected, so it is necessary to process the vibration signal.

B. SIGNAL PROCESSING

According to the features of fault signal, a joint PSO-MCKD-VMD-FSK algorithm is proposed to extract fault features. The PSO is mainly used to optimize the initial set filtering length L and the deconvolution period T in MCKD. And optimize the decomposition mode parameter K and penalty parameter α of VMD. Firstly, MCKD is used to reduce noise and enhance signal of the original signal; secondly, VMD algorithm is used to decompose the signal after preprocessing; then, components are screened by Pearson correlation coefficient method; finally, FSK and envelope demodulation method are used to distinguish fault characteristics, and the specific processing flow is shown in Figure 14.

1) PSO

PSO uses the sharing of information among individuals in a group to make the movement of the whole group produce an evolutionary process from disorder to order in the problem solution space, so as to obtain the optimal solution. The basic calculation process is as follows:

(1) Initialize the population and set basic parameters such as the maximum genetic number (T), inertial factor (ϖ), learning factors (c1, c2), etc.

(2) According to the objective function, the fitness function of particles is calculated, and the local optimal solution of particle swarm is calculated.

(3) The speed and position of particles in the population are optimized according to the local optimal solution.

(4) Determine whether the termination condition is satisfied, and terminate the iteration if the requirements are met, otherwise return to step (2). The update formula of particle
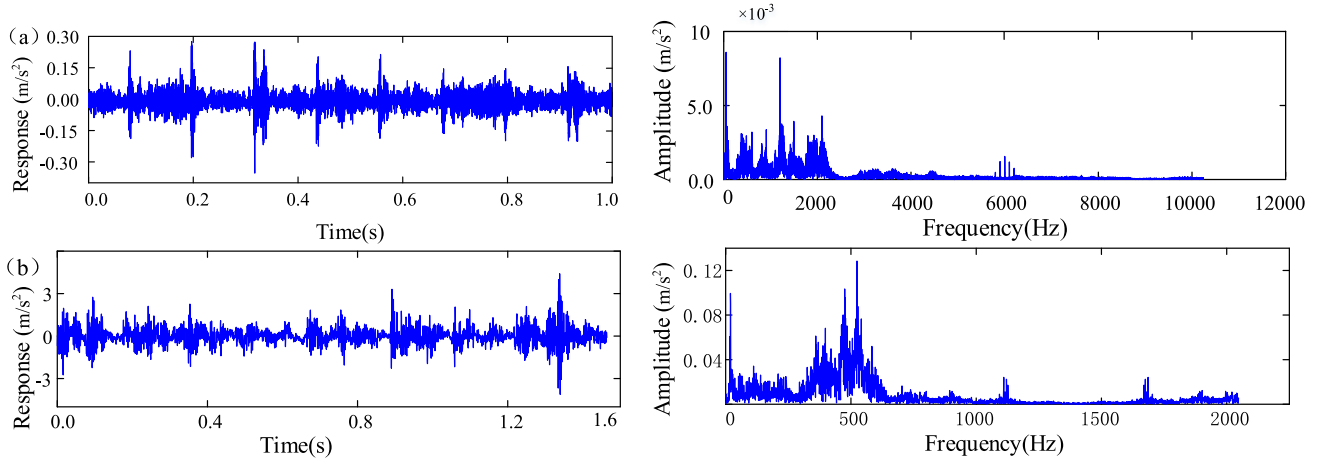
FIGURE 13. The diagram of experimental vibration response. (a) System with gear crack. (b) System with shaft crack.
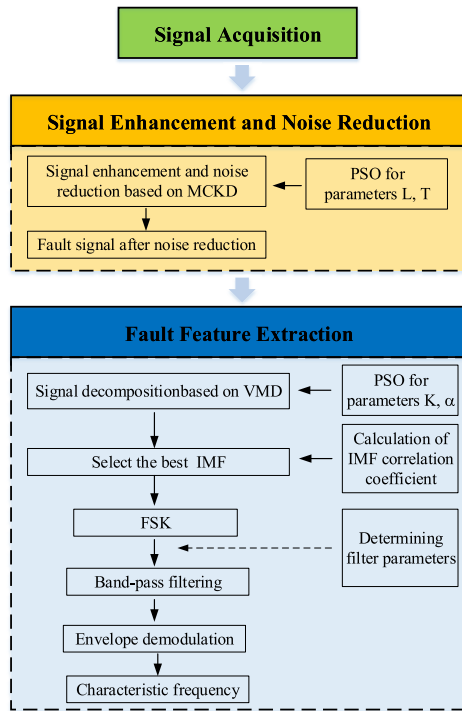

FIGURE 14. Flow chart of fault diagnosis.

speed and position in particle swarm algorithm is as follows:

$$v_{ip}(n+1) = \omega v_{ip}(n) + c_1 r_1(d_{ip}(n) - x_{ip}(n))$$
$$+ c_2 r_2(d_{gp}(n) - x_{ip}(n)) \qquad (37)$$
$$x_{ip}(n+1) = x_{ip}(n) + v_{ip}(n+1) \qquad (38)$$

where, $x_{ip}(n)$ is the p-dimensional position of the nth iteration of particle i; $v_{ip}(n)$ is the p-dimensional speed of the nth iteration of particle i; $d_{ip}(n)$ is the individual extreme point position of the nth iteration of particle i; $d_{gp}(n)$ is the group extreme point position of the nth iteration of particle i; c_1 and

c_2 are learning factors; ϖ is inertia coefficient; r_1 and r_2 are random numbers between [0,1].

In this paper, PSO is used to search the parameters combination of the MCKD algorithm [filter length: L, deconvolution period: T] and the VMD algorithm [decomposition mode parameter: K, penalty term parameter: α], so as to realize the adaptive parameter selection.

2) MCKD

The essence of the MCKD algorithm is to find a FIR filter, and recover the input signal Y through the output signal x, as follows:

$$y = f * x = \sum_{k=1}^{L} f_k x_{n-k+1} \qquad (39)$$

where, $f = [f_1 f_2 \cdots f_L]^T$ is the filter coefficient of length L In order to highlight the continuous sharp pulse in the deconvolution result, the algorithm takes the correlation kurtosis of the signal as the evaluation standard, and maximizes the correlation kurtosis as the final objective function, which is expressed as follows

$$O(CK_M(T)) = \frac{\sum_{n=1}^{N} (\prod_{m=0}^{M} y(n-mT))^2}{(\sum_{n=1}^{N} y_n^2)^{M+1}} \qquad (40)$$

In order to obtain the optimal inverse filter f coefficient, the first derivative of the objective function is defined as zero, namely:

$$\frac{d}{df_k} CK_M(T) = 0, \quad k = 1, 2, \cdots, L \qquad (41)$$

Based on this, the best filter coefficient is obtained

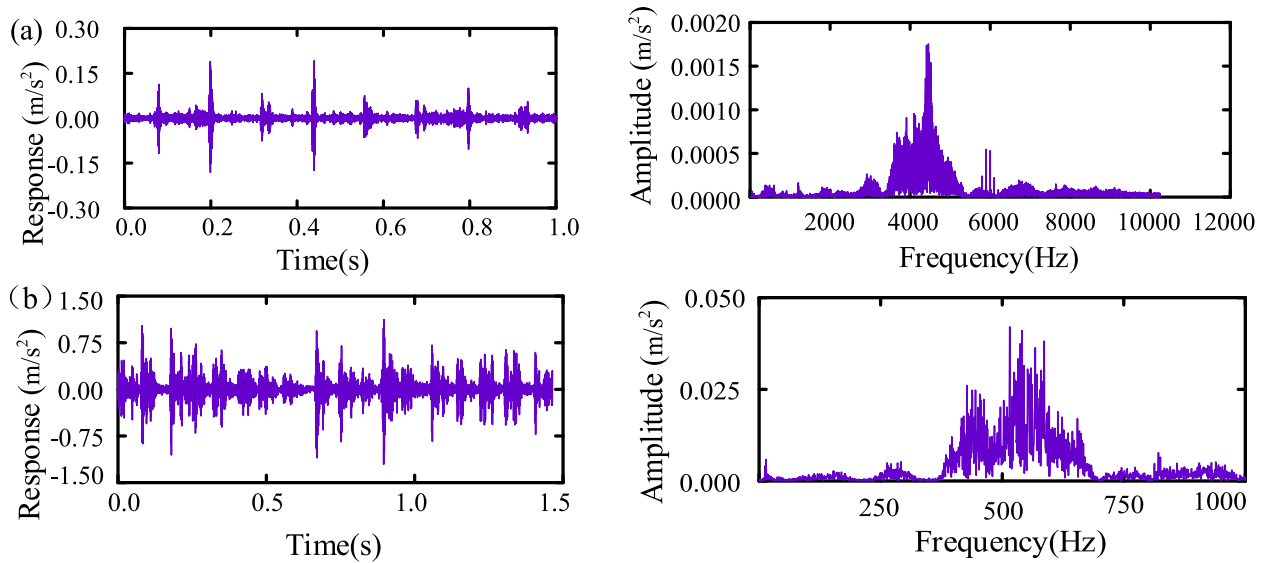$$f = \frac{\|y^2\|}{2\|\beta\|^2}(X_o X_o^T)^{-1} \sum_{m=0}^{M} (X_{mT}\alpha_m) \qquad (42)$$

FIGURE 15. Time-frequency diagram after MCKD processing. (a) System with gear crack. (b) System with shaft crack.

where, $\alpha_0 = [y_1 y_{1-T}^2 \ y_2 y_{2-T}^2 \ \cdots \ y_N y_{N-T}^2]^T$, $\alpha_1 = [y_{1-T} y_1^2 \ y_{2-T} y_2^2 \ \cdots \ y_{N-T} y_N^2]^T$ $\beta = [y_1 y_{1-T} \ y_2 y_{2-T} \ \cdots \ y_N y_{N-T}]^T$,

$$
X_r = \begin{bmatrix}
x_{1-r} & x_{2-r} & x_{3-r} & \cdots & x_{N-r} \\
0 & x_{1-r} & x_{1-r} & \cdots & x_{N-1-r} \\
0 & 0 & x_{1-r} & \cdots & x_{N-2-r} \\
\vdots & \vdots & \vdots & \ddots & \vdots \\
0 & 0 & 0 & \cdots & x_{N-L-r-1}
\end{bmatrix}_{L \times N} \quad (43)
$$

The specific calculation steps of the MCKD algorithm are as follows

(1) Determine the length L of the filter, the number of conversions M and the period T of the signal.

(2) Calculate the X_o, X_{ot} and X_{mT} of the original signal $x(n)$

(3) Find the filtered output signal y (n).

(4) Update the filter coefficients.

If the signal $\Delta CK_M(T) < \varepsilon$ before and after filtering, stop the iteration and jump back to step (3).

The deconvolution signal y of the actual acquisition signal x can be obtained by substituting the obtained inverse filter coefficient into equation (2).

Set the combined parameter [L, T] in combination with PSO, the noise reduction result of vibration signal with gear crack is shown in Figure 15(a), with L = 22, t = 22; the noise reduction result of vibration signal with shaft crack is shown in Figure 15(b), with L = 16, T = 168.

3) VMD

VMD decomposes the different frequency components of complex vibration signals from high to low, and generates a series of components with different frequency scales, which can separate the main components representing the fault state.

The VMD decomposes the vibration signal f(t) into k modal components with a center frequency of ω_k. For this purpose, an optimal variation model is constructed as follows

$$
\begin{cases}
\min\limits_{\{u_k\},\{\omega_k\}} \left\{ \sum_k \left\| \frac{\partial}{\partial t} \left[\left(\delta(t) + \frac{j}{\pi t} \right) * u_k(t) \right] e^{-j\omega_k t} \right\|_2^2 \right\} \\
s.t. \sum_{k=1}^{K} u_k(t) = f(t)
\end{cases} \quad (44)
$$

When solving the problem, the second penalty factor α and Lagrange multiplier $\lambda(t)$ are introduced to transform the original model into a non-constrained variation problem, and an extended Lagrange expression formula (45) is obtained

$$
\begin{aligned}
L(\{u_k\}, \{w_k\}, \lambda) = {} & \alpha \sum_k \left\| \partial_t \left[(\delta(t) + \frac{j}{\pi t}) * u_k(t) \right] e^{-jwkt} \right\|_2^2 \\
& + \left\| f(t) - \sum_k u_k(t) \right\|_2^2 \\
& + \langle \lambda(t), f(t) - \sum_k u_k(t) \rangle \quad (45)
\end{aligned}
$$

Thereafter, the multiplier algorithm is used to alternate the direction of solution (45), iterate continuously and update alternately u_k^{n+1}, w_k^{n+1} and w_k^{n+1} as equation (46-48), in order to search for the "saddle point" of extended Lagrange.

$$
u_k^{n+1}(w) = \frac{f(w) - \sum_{j \neq k} u_j(w) + \frac{\lambda(w)}{2}}{1 + 2\alpha(w - w_k)^2} \quad (46)
$$

$$
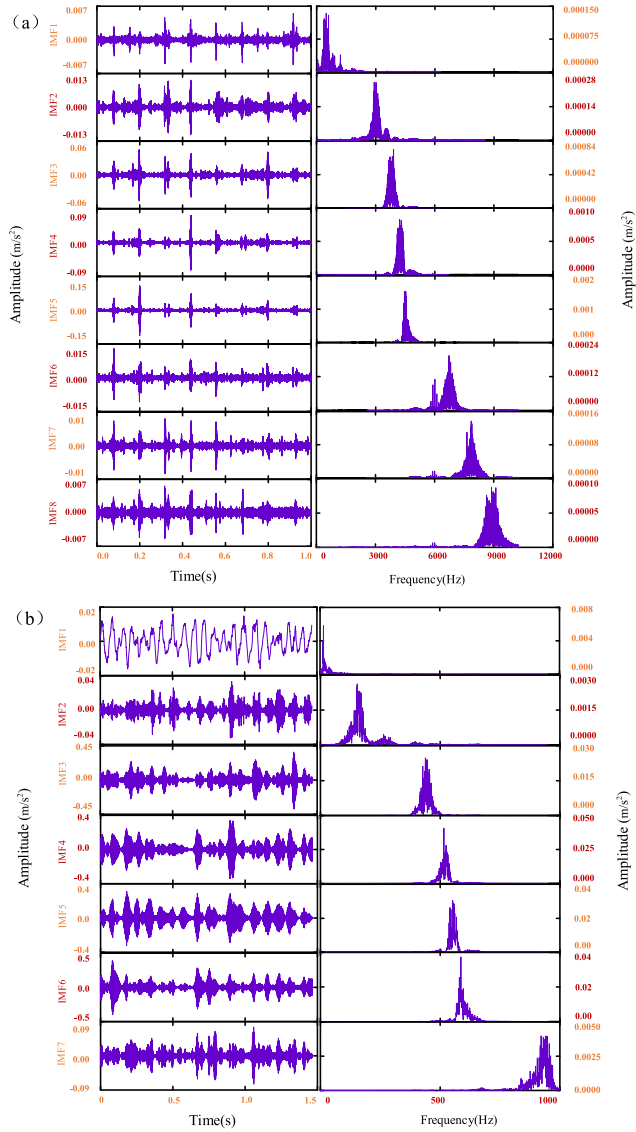w_k^{n+1} = \frac{\int_0^\infty w |u_k(w)|^2 dw}{\int_0^\infty |u_k(w)|^2 dw} \quad (47)
$$

FIGURE 16. Processing results by VMD. (a) System with gear crack. (b) System with shaft crack.

$$\lambda^{n+1}(w) = \lambda^{n}(w) + \tau[f(w) - \sum_{k} u_k^{n+1}(w)] \quad (48)$$

Setting combination parameters $[K, \alpha]$ with PSO, the decomposition results of vibration signal with gear crack are shown in Figure 16(a), with $K = 8$, $\alpha = 2526$; the decomposition results of vibration signal with shaft crack are shown in Figure 16(b), with $K = 7$, $\alpha = 3473$.

Subsequently, the VMD components are screened by Pearson correlation coefficient, and the component with the largest correlation coefficient value is selected as the optimal component. In order to realize the fast calculation of spectral kurtosis, the optimal component of VMD is analyzed by FSK in reference [26], and the signal envelope diagram is obtained as shown in the figure. From figure 17, it can be seen that both fault frequencies are the rotation frequency where the fault occurs, which is consistent with the theoretical analysis.
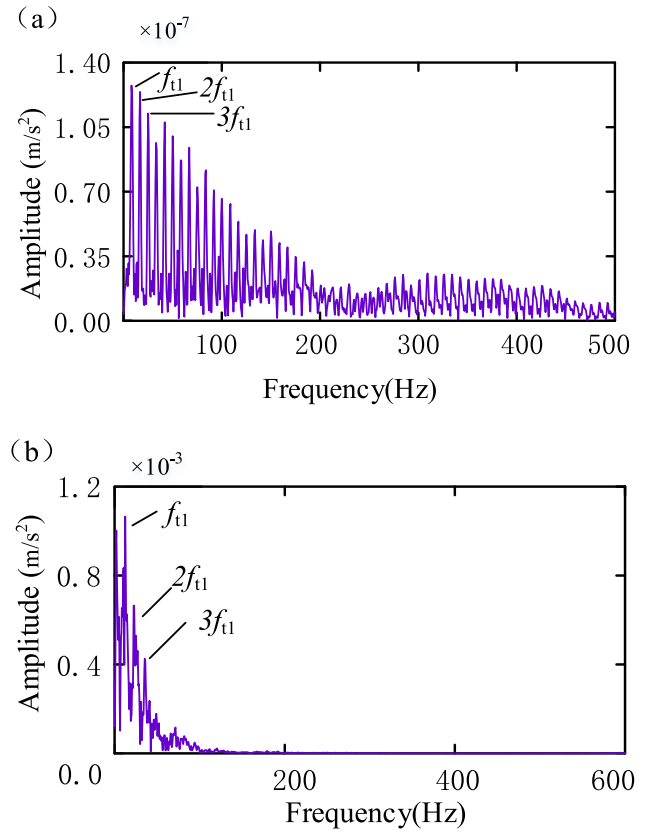

FIGURE 17. The signal envelope spectrum. (a) The signal envelope spectrum for gear crack. (a) The signal envelope spectrum for shaft crack.

V. ANALYSIS OF INFLUENCING FACTORS AND DIFFERENCES

A. EFFECT OF CRACK DEPTH ON VIBRATION CHARACTERISTICS

As in the previous section, the effect of crack depth on the system vibration response is investigated at an input shaft speed of 50 rad/s and a load of 100N · m. Figure 18 shows a three-dimensional graph of the crack depth and vibration response. Figure 18(a) shows a graph of the relationship between the crack depth and the time-domain history under the gear crack fault. Figure 18(b) shows a graph of the relationship between the crack depth and the time-domain history under the shaft crack fault. Figure 18(c) shows a graph of the relationship between the crack depth and the frequency-domain under the gear crack fault. Figure 18(d) shows a graph of the relationship between the crack depth and the frequency-domain under the shaft crack fault.

Figures 18(a) and 18(b) show that as the crack depth positively correlated with the two fault responses, the deeper the root crack, the stronger the system impact; the deeper the shaft crack, the more apparent the system time-domain modulation phenomenon.

Figures 18(c) and 18(d) show that as the gear crack deepens, the sideband near its meshing frequency become more obvious; as the shaft crack fault become more serious, the frequency conversion and its frequency doubling corresponded
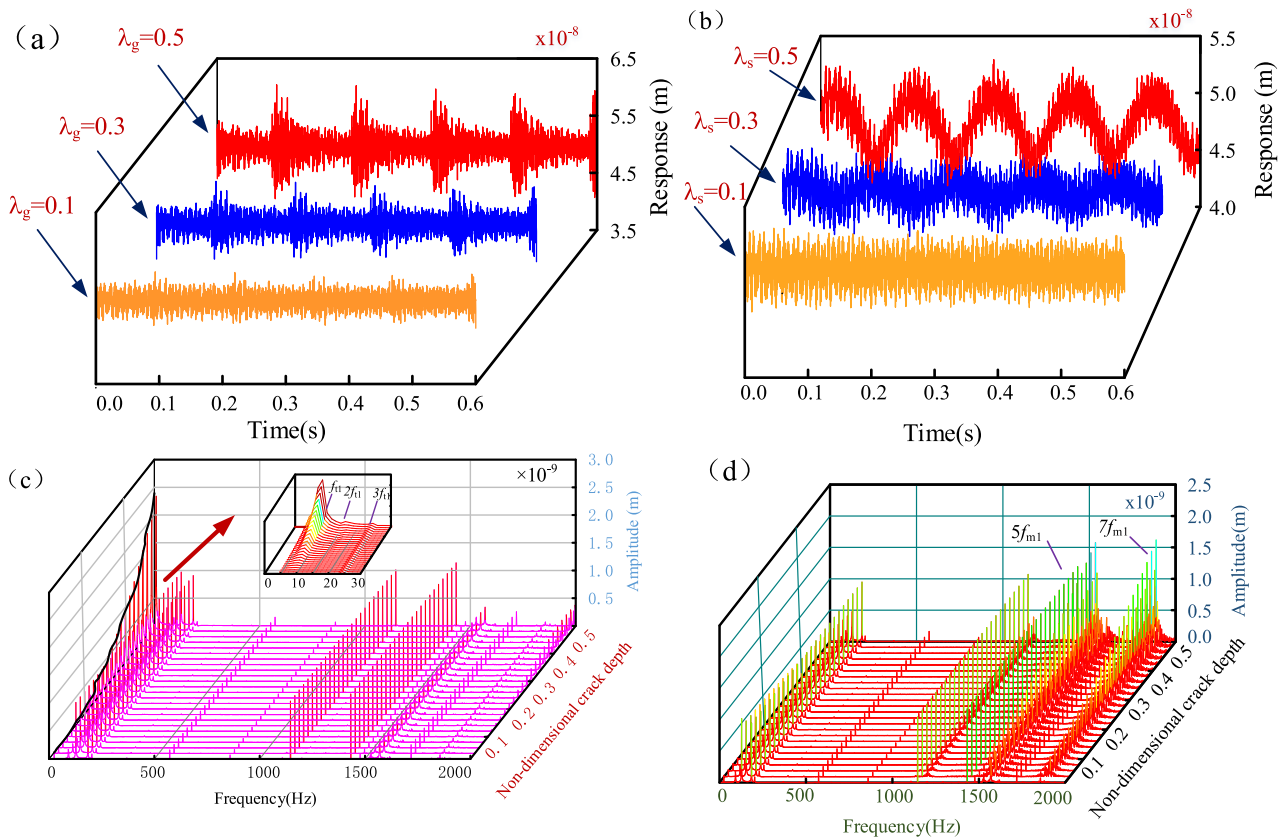
FIGURE 18. Three-dimensional spectrum diagram. (a) Time domain response varies with crack depth (gear crack). (b) Time domain response varies with crack depth (shaft crack). (c) Frequency response varies with crack depth (gear crack). (d) Frequency response varies with crack depth (shaft crack).

to the fault shaft becoming more obvious, and the f_{t1} is the most significant; and the amplitude of $2f_{t1}$ become more apparent as the crack depth increases, while the amplitude of $3f_{t1}$ slowly increases.

B. EFFECT OF INPUT SPEED

In order to explore the characteristics of vibration response during system speed-up under different fault conditions, taking into account the flexibility of shaft section, the whole acceleration process keeps the load torque of 100 N · m. The crack parameter is $\lambda_{g,s} = 0.5$, which is located in the 6th element. The calculated speed-amplitude curve is shown in the Fig.19.

Figure 19 shows that system resonance can be caused when the external excitation frequency (frequency conversion, engagement frequency of two-stage gear, and its frequency multiplication) of the system is close to the natural system frequency. The peak value of point A corresponds to the input speed of 380 rad/s, and $2f_{m2}$ is close to the f_{n3}; Point B corresponds to a speed of 560 rad/s, and the $2f_{m1}$ approximates the f_{n8}; at point C, the corresponding speed is 780 rad/s, and the f_{n1} is close to the first natural system frequency; and at point D, the corresponding speed is 840 rad/s, and the f_{m2} is close to the f_{n3}. Simultaneously,
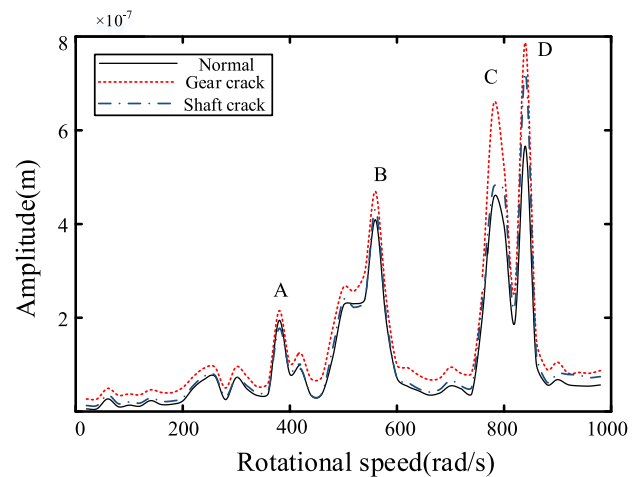

FIGURE 19. Vibration amplitudes versus input speeds.

the system failure; mean that the system flexibility of the system is enhanced, so that the response amplitude is greater than the normal response of the system, and, at the same speed, the response amplitude caused by the gear crack is greater than the response amplitude caused by the shaft crack.
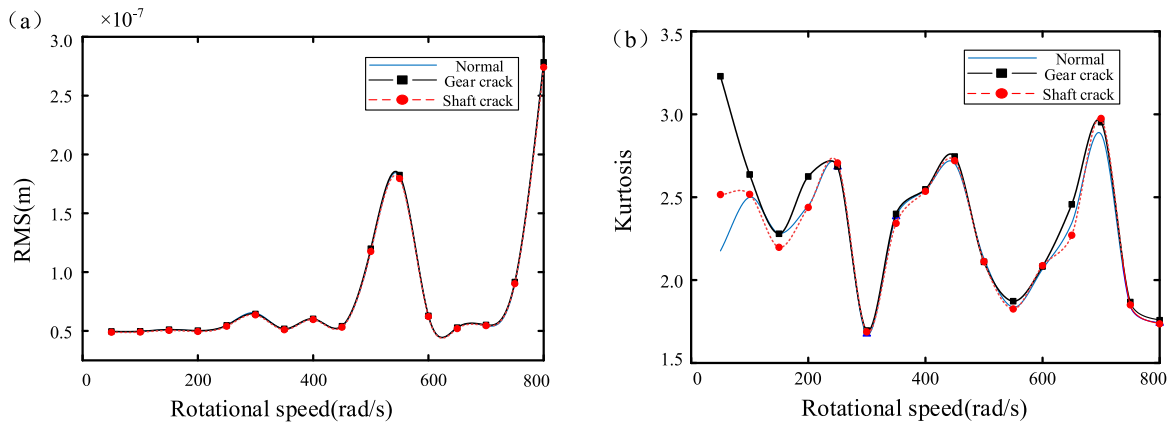
FIGURE 20. Time domain statistical indicators changes with speeds. (a) RMS changes with speeds. (b) Kurtosis changes with speeds.
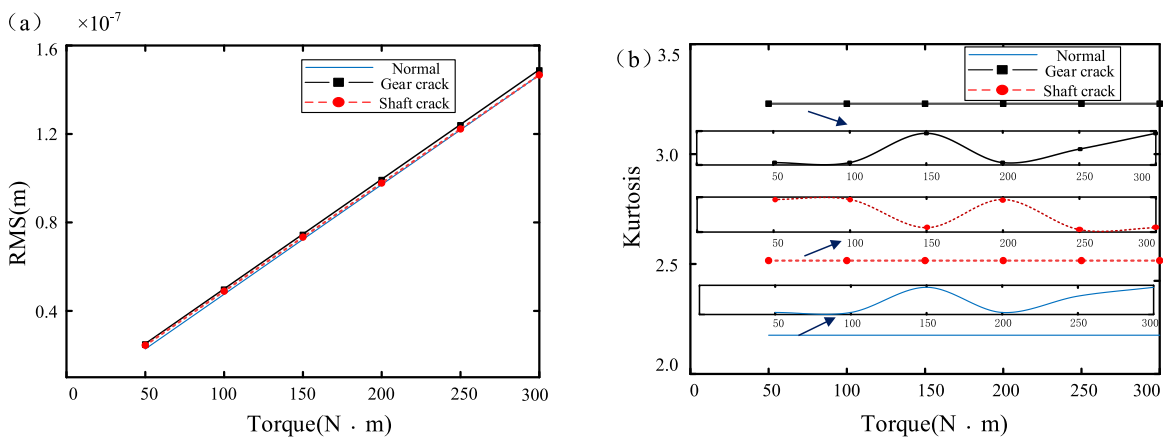

FIGURE 21. Time domain statistical indicators changes with loads. (a) RMS changes with loada. (b) Kurtosis changes with loads.

C. EFFECT OF WORKING CONDITIONS ON FREQUENCY CHARACTERISTICS

Mean square root (RMS) and kurtosis are selected to characterize signal characteristics, in which the mean square root is often used to measure the energy level of vibration time-domain history. The mathematical expression is

$$RMS = \sqrt{\frac{1}{N} \sum_{n=1}^{N} (x(n) - \bar{x})^2} \qquad (49)$$

where, $\bar{x} = \frac{1}{N} \sum_{n=1}^{N} x(n)$.

Kurtosis is a numerical statistic on the distribution of vibration signals, which can reflect the fault impact component in the vibration signals. It is calculated as follows

$$Kurtosis = \frac{\frac{1}{N} \sum_{n=1}^{N} (x(n) - \bar{x})^4}{\left[\frac{1}{N} \sum_{n=1}^{N} (x(n) - \bar{x})^2 \right]^2} \qquad (50)$$

And, in order to explore the correlation between variable operating conditions and RMS and kurtosis index, further analysis of signal characteristics with speed and load changes.

Under the condition of a load torque of 100 N · m, he RMS change trend, the kurtosis index, and the speed increase are shown in Figure 20. Figure 20(a) shows that t a peak value exists near the speed of 550 rad/s. This is because, at this speed, the $2f_{m1}$ is close to the f_{n8}, resulting in system resonance and raising the RMS peak value. Figure 20(b) shows that the kurtosis index of the three is different when the rotating speed is 50~200rad/s, and the kurtosis index of the three gradually shrank with the increase of rotating speed.

The RMS change trend, the kurtosis index, and load all increase at the speed of 50 rad/s, as shown in Figure 21. The RMS value of the system increases in direct proportion o the load torque increases. The load increases, means that the RMS value of the gear fault system gradually became greater than that of the shaft fault system, but the overall difference is small. For example, when the load is 250N · m, the difference between the two is only 1.66 μm. In contrast,

FIGURE 23. IMF energy distribution in different states.

the system, and crack generation makes the stiffness mutation more apparent, which shows that the kurtosis value of the fault system with the gear cracks is larger.

D. VMD DECOMPOSITION OF VIBRATION SIGNALS
For VMD decomposition of simulation signal, the principle of close center frequency is used to determine the number of decomposition layers. Here, it is determined that the number of decomposition layers K = 4, the default value of penalty factor α is 2000, $\tau = 0$, and the decomposition result is shown in Figure 22.

Figure 22(a) shows that the overall distribution of the normal system vibration signal is relatively stable; Figure 22(b) shows is the decomposition diagram of the vibration signal of the system with the gear crack fault, in which the components of IMF2, IMF3, and IFM4 take the first stage gear meshing frequency as the center frequency, and different degrees of sidebands near the center frequency exists. The more obvious the sideband is, the larger the proportion of impact components in the corresponding time-domain component is; Figure 22(c) is the vibration signal decomposition diagram of the fault system with the shaft cracks. IMF1 represents the main component in the fault state of the shaft cracks, that is, the frequency component. At this time, the IMF1time-domain component has obvious frequency conversion modulation, which shows as "simple harmonic".

The energy distribution of signals in different frequency bands is affected because the different weakening mechanisms of the system stiffness were caused by different faults. To explore the energy distribution difference of different faults, the energy of different frequency bands is extracted for analysis.

The energy of the ith IMF component can be expressed as

$$E_i = \int_{-\infty}^{+\infty} (x(n))^2 dt \qquad (51)$$

Thus, the energy distribution coefficients of three states (normal, including gear cracks, including shaft cracks) are
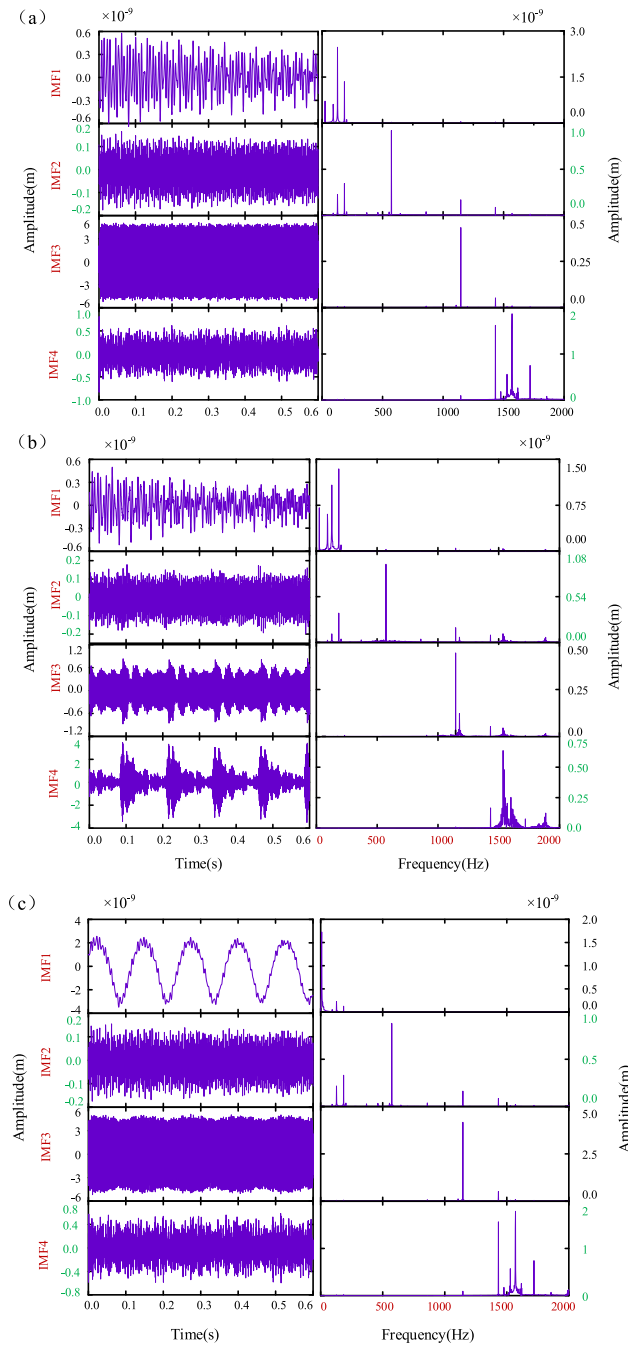
FIGURE 22. Processing results by VMD (simulation signal). (a) Normal. (b) System with gear crack. (c) System with shaft crack.

the kurtosis values of different systems are different at low speed, but with an increasing load, the kurtosis of each system is not obvious, only exhibiting a small range of fluctuations. When the load is 50N · m, the kurtosis of the fault system with the shaft crack is 15.6% higher than that of the normal system, and the kurtosis of the fault system with the gear crack is 48.4% higher than that of the normal system. This demonstrates that the impact phenomenon caused by gear failure is more significant, because the single and double alternation of low-speed gear is the main excitation source of
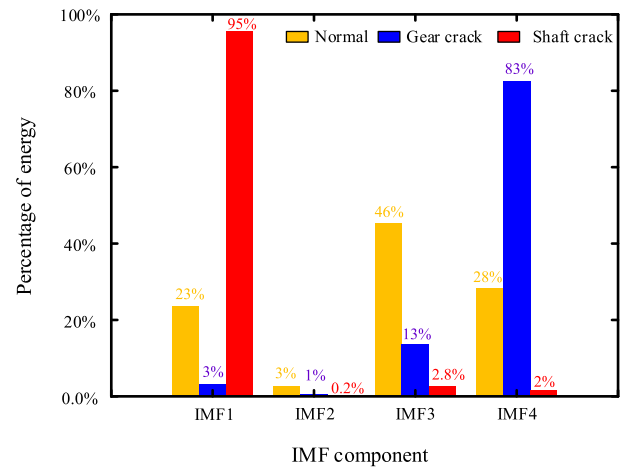
constructed

$$[e_1, e_2, \cdots, e_n] = [E_1/E_{all}, E_2/E_{all}, \cdots, E_n/E_{all}] \quad (52)$$

where, $E_{all} = \sum_i^n E_i$.

The distribution coefficients of the three state components are calculated as shown in Figure 23.

In the normal system, the energy distribution is more uniform, the uncertainty is greater, and the energy entropy of the whole system is larger than that in the fault state; the vibration signal of the fault system with gear crack is concentrated in the frequency band where the meshing frequency exists, mainly concentrated around $5f_{m1}$ and $7f_{m1}$; and the vibration signal energy of IMF1 of the fault system with shaft crack is 95% of the whole system, indicating that the energy is the main focus on low frequency areas.

VI. CONCLUSION

In this study, the meshing stiffness of a gear with crack fault is calculated via FEM, and the stiffness matrix of a shaft element with a breathing crack is derived. Considering shaft flexibility, the finite element dynamic models of the secondary gear drive system with the gear and shaft cracks are established respectively. Finally, different fault source vibration responses are compared and the influencing factors are analyzed by combining the tests. The conclusions are as follows:

(1) Affected by the gear crack, the vibration response of the system shows periodic impacts in the time domain. In the spectrum, side-frequency modulation occurs mainly near the meshing frequency and its multiplication. Also under the influence of the shaft crack, the time domain presents as "simple harmonic" modulation, while in the frequency domain, it manifests as frequency conversion and frequency

multiplication of the faulty shaft in the low-frequency region. Both fault modulation periods are the reciprocal of the shaft rotation frequency where the fault is located.

(2) The gear crack fault mainly affects the low-order natural system frequency, especially the low-order natural frequency corresponding to the torsional vibration mode. The difference is that shaft crack fault has a greater influence on the natural frequencies above the 10th order (including the 10th order), and its effect is not limited to the natural frequencies corresponding to the torsional vibration modes.

(3) The PSO-MCKD-VMD-FSK method effectively extracts the two fault characteristics in this study. Results are consistent with the theoretical analysis, and this method effectively resists the influence of noise on the signal.

(4) The system frequency characteristics of different source faults are different, and cracks affect the energy distribution of the system. The gear cracks concentrate vibration energy mainly near the meshing frequency and its multiplication, while under the effect of the shaft crack; the system energy mainly concentrates on the low-frequency area.

APPENDIX
THE ELEMENT MATRICES OF SHAFT AND GEAR PAIR

$$M_e = \frac{\pi r^3 l}{6} \begin{bmatrix} 2 & 0 & 0 & 1 & 0 & 0 \\ 0 & 2 & 0 & 0 & 1 & 0 \\ 0 & 0 & \dfrac{2J}{\pi r^2} & 0 & 0 & \dfrac{J}{\pi r^2} \\ 1 & 0 & 0 & 2 & 0 & 0 \\ 0 & 1 & 0 & 0 & 2 & 0 \\ 0 & 0 & \dfrac{J}{\pi r^2} & 0 & 0 & \dfrac{2J}{\pi r^2} \end{bmatrix}$$

where, l is Shaft element length, J is polar moment of inertia of shaft section to center of circle the equation can be derived,

$$K_e = \begin{bmatrix} \dfrac{G \cdot \pi r^2}{\lambda \cdot l} & 0 & 0 & -\dfrac{G \cdot \pi r^2}{\lambda \cdot l} & 0 & 0 \\ 0 & \dfrac{G \cdot \pi r^2}{\lambda \cdot l} & 0 & 0 & -\dfrac{G \cdot \pi r^2}{\lambda \cdot l} & 0 \\ 0 & 0 & \dfrac{G \cdot J}{l} & 0 & 0 & -\dfrac{G \cdot J}{l} \\ -\dfrac{G \cdot \pi r^2}{\lambda \cdot l} & 0 & 0 & \dfrac{G \cdot \pi r^2}{\lambda \cdot l} & 0 & 0 \\ 0 & -\dfrac{G \cdot \pi r^2}{\lambda \cdot l} & 0 & 0 & \dfrac{G \cdot \pi r^2}{\lambda \cdot l} & 0 \\ 0 & 0 & -\dfrac{G \cdot J}{l} & 0 & 0 & \dfrac{G \cdot J}{l} \end{bmatrix}$$

$$K_m = \begin{bmatrix} k_m \sin^2 \alpha & k_m \sin \alpha \cos \alpha & -k_m \sin \alpha r_1 & -k_m \sin^2 \alpha & -k_m \sin \alpha \cos \alpha & -k_m \sin \alpha r_2 \\ k_m \sin \alpha \cos \alpha & k_m \cos^2 \alpha & -k_m \cos \alpha r_1 & -k_m \sin \alpha \cos \alpha & -k_m \cos^2 \alpha & -k_m \cos \alpha r_2 \\ -k_m \sin \alpha r_1 & -k_m \cos \alpha r_1 & k_m r_1^2 & k_m \sin \alpha r_1 & k_m \cos \alpha r_1 & k_m r_1 r_2 \\ -k_m \sin^2 \alpha & -k_m \sin \alpha \cos \alpha & k_m \sin \alpha r_1 & k_m \sin^2 \alpha & k_m \sin \alpha \cos \alpha & k_m \sin \alpha r_2 \\ -k_m \sin \alpha \cos \alpha & -k_m \cos^2 \alpha & k_m \cos \alpha r_1 & k_m \sin \alpha \cos \alpha & k_m \cos^2 \alpha & k_m \cos \alpha r_2 \\ -k_m \sin \alpha r_2 & -k_m \cos \alpha r_2 & k_m r_1 r_2 & k_m \sin \alpha r_2 & k_m \cos \alpha r_2 & k_m r_2^2 \end{bmatrix}$$

as shown at the bottom of previous page. where, G is shear modulus, λ is cross section shape coefficient of shaft element the equation can be derived, as shown at the bottom of previous page.

REFERENCES

[1] F. Chaari, T. Fakhfakh, and M. Haddar, "Analytical modelling of spur gear tooth crack and influence on gearmesh stiffness," *Eur. J. Mech.-A/Solids*, vol. 28, no. 3, pp. 461–468, May 2009.

[2] Z. Chen and Y. Shao, "Dynamic simulation of spur gear with tooth root crack propagating along tooth width and crack depth," *Eng. Failure Anal.*, vol. 18, no. 8, pp. 2149–2164, Dec. 2011.

[3] I. Howard, S. Jia, and J. Wang, "The dynamic modelling of a spur gear in mesh including friction and a crack," *Mech. Syst. Signal Process.*, vol. 15, no. 5, pp. 831–853, Sep. 2001.

[4] D. C. H. Yang and J. Y. Lin, "Hertzian damping, tooth friction and bending elasticity in gear impact dynamics," *J. Mech. Transmiss. Automat. Des.*, vol. 109, no. 2, p. 189, 1987.

[5] X. Tian, *Dynamic Simulation for System Response of Gearbox Including Localized Gear Faults*. Edmonton, AB, Canada: Univ. of Alberta Edmonton, 2004.

[6] G. Litak and M. I. Friswell, "Dynamics of a gear system with faults in meshing stiffness," *Nonlinear Dyn.*, vol. 41, no. 4, pp. 415–421, Sep. 2005.

[7] S. Wu, M. J. Zuo, and A. Parey, "Simulation of spur gear dynamics and estimation of fault growth," *J. Sound Vibrat.*, vol. 317, nos. 3–5, pp. 608–624, Nov. 2008.

[8] Z. Meng, G. Shi, and F. Wang, "Vibration response and fault characteristics analysis of gear based on time-varying mesh stiffness," *Mechanism Mach. Theory*, vol. 148, Jun. 2020, Art. no. 103786.

[9] A. Saxena, M. Chouksey, and A. Parey, "Measurement of FRFs of coupled geared rotor system and the development of an accurate finite element model," *Mechanism Mach. Theory*, vol. 123, pp. 66–75, May 2018.

[10] R. Gasch, *Dynamic Behavior of a Simple Rotor With a Cross Sectional Crack*. London, U.K.: Vibrations in Rotating Machinery, 1976, pp. 123–128.

[11] A. D. Dimarogonas and C. A. Papadopoulos, "Vibration of cracked shafts in bending," *J. Sound Vib.*, vol. 91, no. 4, pp. 583–593, Dec. 1983.

[12] I. W. Mayes and W. G. R. Davies, "Analysis of the response of a multi-rotor-bearing system containing a transverse crack in a rotor," *J. Vib. Acoust. Stress Rel. Des.*, vol. 106, no. 1, p. 139, 1984.

[13] O. S. Jun, H. J. Eun, Y. Y. Earmme, and C.-W. Lee, "Modelling and vibration analysis of a simple rotor with a breathing crack," *J. Sound Vib.*, vol. 155, no. 2, pp. 273–290, Jun. 1992.

[14] J. M. Gao and X. M. Zhu, "Research on the breathing model of crack on rotating shaft," *Chin. J. Appl. Mech.*, vol. 9, no. 1, pp. 108–112, 1992.

[15] T. H. Patel and A. K. Darpe, "Influence of crack breathing model on nonlinear dynamics of a cracked rotor," *J. Sound Vib.*, vol. 311, nos. 3–5, pp. 953–972, Apr. 2008.

[16] M. A. AL-Shudeifat, "On the finite element modeling of the asymmetric cracked rotor," *J. Sound Vib.*, vol. 332, no. 11, pp. 2795–2807, May 2013.

[17] M. A. Al-Shudeifat and E. A. Butcher, "New breathing functions for the transverse breathing crack of the cracked rotor system: Approach for critical and subcritical harmonic analysis," *J. Sound Vib.*, vol. 330, no. 3, pp. 526–544, Jan. 2011.

[18] Z. Lu, L. Hou, Y. Chen, and C. Sun, "Nonlinear response analysis for a dual-rotor system with a breathing transverse crack in the hollow shaft," *Nonlinear Dyn.*, vol. 83, nos. 1–2, pp. 169–185, Jan. 2016.

[19] D. Yu, "Fault diagnosis approach for gears based on EMD and SVM," *Chin. J. Mech. Eng.*, vol. 41, no. 1, pp. 140–144, 2005.

[20] C. Junsheng, Y. Yi, and Y. Yu, "Application of spectral kurtosis approach based on local mean decomposition (LMD) in ear faul diagnosis," *J. Vib. Shock*, vol. 31, no. 18, pp. 20–23 and 54, 2012.

[21] Y. Yang, J. Cheng, and K. Zhang, "An ensemble local means decomposition method and its application to local rub-impact fault diagnosis of the rotor systems," *Measurement*, vol. 45, no. 3, pp. 561–570, Apr. 2012.

[22] J. Hong, Z. Xiangfeng, and Z. Xiaodong, "Gear early weak fault feature enhancement in dual vector time-time domain," *J. Vib., Meas. Diagnosis*, vol. 38, no. 6, pp. 1161–1168 and 1291, 2018.

[23] K. Dragomiretskiy and D. Zosso, *Variational Mode Decomposition*. Piscataway, NJ, USA: IEEE Press, 2014.

[24] G. L. McDonald, Q. Zhao, and M. J. Zuo, "Maximum correlated kurtosis deconvolution and application on gear tooth chip fault detection," *Mech. Syst. Signal Process.*, vol. 33, pp. 237–255, Nov. 2012.

[25] J. Antoni, "Fast computation of the kurtogram for the detection of transient faults," *Mech. Syst. Signal Process.*, vol. 21, no. 1, pp. 108–124, Jan. 2007.

[26] A. Francis and C. Muruganantham, "An adaptive denoising method using empirical wavelet transform," *Int. J. Comput. Appl.*, vol. 117, no. 21, pp. 18–20, May 2015.
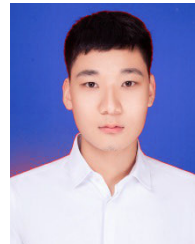
YONG SHEN was born in Hunan, China, in 1995. He is currently pursuing the M.S. degree in mechanical engineering with Xinjiang University, Urumqi, China. His main research interests are gear system dynamics and signal processing.

XIANGFENG ZHANG received the B.S., M.S., and Ph.D. degrees in mechanical engineering from Xinjiang University, Urumqi, China, in 2008, 2011, and 2017, respectively.

He is currently an Associate Professor with the School of Mechanical Engineering, Xinjiang University. His main research interests are mechanical system fault diagnosis and signal processing.

HONG JIANG received the M.S. and Ph.D. degrees in mechanical engineering from Xinjiang University, Urumqi, China, in 2006 and 2012, respectively.

He is currently a Professor with the School of Mechanical Engineering, Xinjiang University. His main research interests are mechanical system fault diagnosis and nondestructive testing.

JIANXING ZHOU was born in Xinjiang, China, in 1982. He received the Ph.D. degree in mechanical engineering from Northwest Polytechnical University, Xian, China, in 2013. From 2013 to 2018, he was an Assistant Professor with the College of Mechanical Engineering. Since 2019, he has been a Professor with the College of Mechanical Engineering, Xinjiang University.

SHUAI QIAO was born in Henan, China, in 1995. He is currently pursuing the M.S. degree in mechanical engineering with Xinjiang University, Urumqi, China. Since 2018, he has been working on gear system dynamics. His current research interests include gear system dynamics, vibration, and heat transfer.

TONGWEI MA was born in Gansu, China, in 1994. He is currently pursuing Ph.D. degree in mechanical engineering with Xinjiang University, Urumqi, China. His main research interests are mechanical system fault diagnosis and signal processing.

• • •

CHENGLONG WANG was born in Henan, China, in 1992. He is currently pursuing the M.S. degree in mechanical engineering with Xinjiang University, Urumqi, China. His main research interests are vibration control and the stress analysis of planetary transmission.